

Equation of state and pressure-induced structural changes in mirabilite ($\text{Na}_2\text{SO}_4 \cdot 10\text{H}_2\text{O}$) determined from ab initio density functional theory calculations

Helen E. A. Brand · A. Dominic Fortes ·
Ian G. Wood · Lidunka Vočadlo

Received: 13 May 2009 / Accepted: 11 September 2009
© Springer-Verlag 2009

Abstract We have carried out ab initio calculations using density functional theory to determine the bulk elastic properties of mirabilite, $\text{Na}_2\text{SO}_4 \cdot 10\text{H}_2\text{O}$, and to obtain information on structural trends caused by the application of high pressure up to ~ 60 GPa. We have found that there are substantial isosymmetric discontinuous structural re-organisations at ~ 7.7 and ~ 20 GPa caused by changes in the manner in which the sodium cations are coordinated by water molecules. The low-pressure and intermediate-pressure phases both have sodium in sixfold coordination but in the high-pressure phase the coordination changes from sixfold to sevenfold. These coordination changes force a re-arrangement of the hydrogen-bond network in the crystal. The trend is towards a reduction in the number of hydrogen bonds donated to the sulphate group (from twelve down to six over the range 0–60 GPa) and an increase in hydrogen bonding amongst the Na-coordinated water molecules and the two interstitial water molecules.

Electronic supplementary material The online version of this article (doi:10.1007/s00269-009-0331-1) contains supplementary material, which is available to authorized users.

H. E. A. Brand · A. D. Fortes (✉) · I. G. Wood · L. Vočadlo
Department of Earth Sciences, University College London,
Gower Street, London WC1E 6BT, UK
e-mail: andrew.fortes@ucl.ac.uk

H. E. A. Brand · A. D. Fortes · I. G. Wood · L. Vočadlo
Center for Planetary Sciences at UCL/Birkbeck,
Gower Street, London WC1E 6BT, UK

Present Address:

H. E. A. Brand
CSIRO Minerals, Box 312, Clayton, Bayview Avenue,
Clayton, VIC 3169, Australia
e-mail: helen.brand@csiro.au

Ultimately, we observe proton transfers from the interstitial waters (forming OH^- ions) to two of the Na-coordinated waters (forming a pair of H_3O^+ ions). The equation of state in the athermal limit of the low-pressure phase of mirabilite, parameterised by fitting an integrated form of the third-order Birch-Murnaghan expression to the calculated energy as a function of unit-cell volume, yields the zero-pressure unit-cell volume, $V_0 = 1468.6(9) \text{ \AA}^3$, the incompressibility, $K_0 = 22.21(9) \text{ GPa}$, and the first pressure derivative $K_0' = (\partial K/\partial P)_0 = 5.6(1)$.

Keywords Mirabilite · Ab initio calculations · Incompressibility · Salt hydrates

Introduction

Sodium sulphate decahydrate— $\text{Na}_2\text{SO}_4 \cdot 10\text{H}_2\text{O}$ —is the stable phase in contact with an equilibrium mixture of Na_2SO_4 and H_2O at room temperature and pressure; the synthetic substance is referred to as Glauber's salt, after its first manufacturer (Glauber 1658), and the naturally occurring substance is the mineral mirabilite (see e.g., Palache et al. 1951). Mirabilite forms abundant and widespread deposits on the Earth in association with salt domes and their related hydrocarbon reservoirs (Colman et al. 2002), with dislocations in thrust terrains, as a component of cold desert salt deposits (Keys and Williams 1981) and glacial ice inclusions (Ohno et al. 2006), and as the metasomatic product of the weathering of alkali igneous rocks (Hardie 1991). Commercially, mirabilite has been acknowledged as a possible thermal storage material due to its large latent heat of hydration (Marliacy et al. 2000). Formation of mirabilite is also a significant problem for the construction industry by virtue of its role in the weathering

of building stone with high sodium sulphate content (see e.g., Goudie and Viles 1997; Rijniens et al. 2005; Marzal and Scherer 2008); damage occurs when dissolution of anhydrous Na_2SO_4 produces supersaturated solutions, which then leads to the precipitation of mirabilite in pore spaces. Commonly, the pressure generated by crystallisation of mirabilite exceeds the strength of the building material (Tsui et al. 2003).

The presence of soluble salts such as Na_2SO_4 in chondritic meteorites has led to the suggestion that multiply-hydrated salts such as mirabilite may also dominate the mantles of the icy moons of the Gas Giant planets (Kargel 1991). Evidence to support these models is provided by distorted H_2O absorption bands in the near infrared spectra of these satellites (observed by the Galileo space-craft between 1995 and 2003), interpreted as mixtures of Mg-, Na_2 -, and/or H_2SO_4 -hydrates (e.g., Dalton et al. 2005; Dalton 2007; Orlando et al. 2005), although there is some ambiguity concerning the identity and origin of the non-ice component (Carlson et al. 2007). In order to interpret the observed surface morphologies of the icy moons and to understand their thermal evolution, geophysical models of their interiors must be constructed. To do this we need to know the phase behaviour, thermoelastic, and transport properties of the constituent materials under the appropriate pressure and temperature conditions. There has, therefore, been an interest in measuring the solubility and density of mirabilite at non-ambient conditions (e.g., Hogenboom et al. 1999; Dougherty et al. 2006) to extend earlier high-pressure investigations into the pressure dependence of the ice-mirabilite eutectic in the range from $0 < P < 0.8$ GPa, and $263 < T < 343$ K (Block 1913; Geller 1924; Tammann 1929; Kryukov and Manikhin 1960; Tanaka et al. 1992). Most recently, the metastable compound sodium sulphate heptahydrate has been fully characterised for the first time (Hamilton and Hall 2008; Hall and Hamilton 2008), and sodium sulphate octahydrate has been identified as an exclusively high-pressure phase (Oswald et al. 2009). These results suggest that the phase behaviour in the Na_2SO_4 - H_2O system may be complex; this complexity may have interesting consequences which impact upon the structure and dynamics of large icy planetary bodies.

Given the extraterrestrial significance of various highly hydrated substances, we have been pursuing a programme of research into their phase behaviour and physical properties (Fortes et al. 2006a, b, c, 2007a, b, 2008a, b, 2009; Brand et al. 2009) with the objective of being able to understand better the internal structure and dynamics of large icy moons and to relate these findings to spacecraft observations of their surface geology (e.g., Fortes et al. 2007a). An integral part of this research involves the use of ab initio calculations (Fortes et al. 2006b) and interatomic potential calculations (Brand et al. 2006).

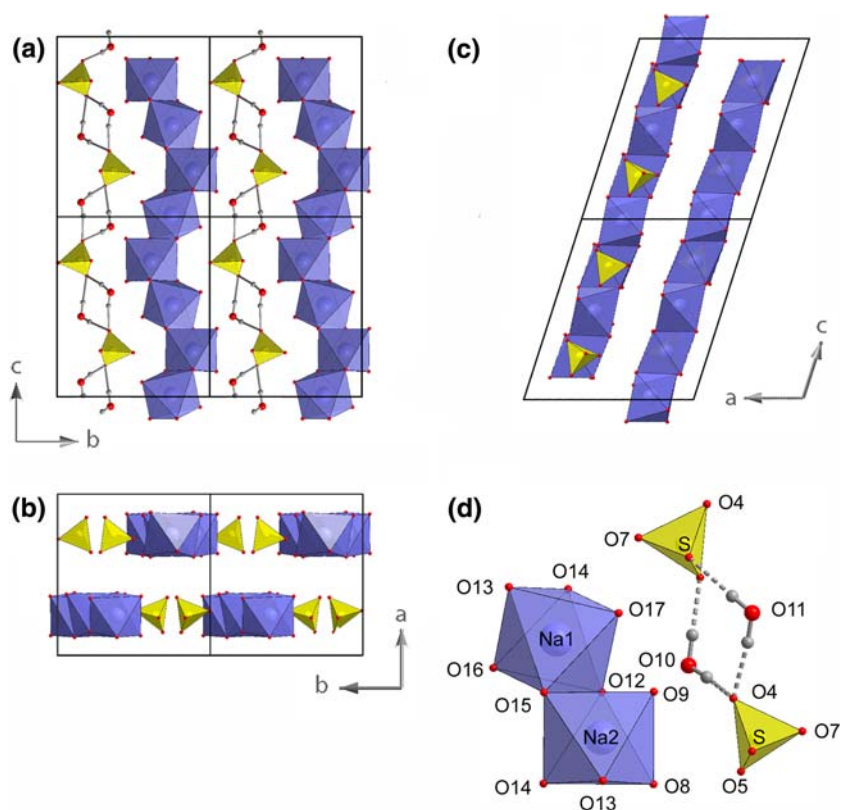
Although the crystal structure and thermal expansion of mirabilite have now been extensively studied as a function of temperature at ambient pressure (Brand et al. 2009), no values of the incompressibility or elastic moduli have yet been published. The objectives of the present study were, therefore, twofold: firstly, to apply ab initio calculations to a relatively difficult problem (i.e., to a substance possessed of low symmetry, with a large unit-cell which contains a very large number of hydrogen atoms) with the aim of determining elastic properties of use in planetary modelling; secondly, to investigate the phase behaviour at high pressure to provide a basis for future high-pressure experimental crystallographic investigations. Our experience of using ab initio density functional theory (DFT) calculations (see “Computational method”) on heavily hydrogen-bonded materials shows that excellent agreement with experimental quantities may be obtained even though the correct physics of van der Waals interactions is not formally accommodated within the framework of DFT. However, in such materials the very weak dependence of the total energy upon the system variables tends to result in a very flat total-energy hypersurface, populated by shallow minima; hence, for example, certain calculated properties are relatively noisy and the uncertainties in fitted parameters may be larger than those obtained in smaller covalently bonded systems.

The paper is arranged as follows: in “Computational method” we describe the computational method, paying particular attention to how the disorder in the mirabilite crystal structure was handled within our static calculations; the results and analysis of the calculations are reported in “Results”, “Discussion” discusses the results and finally, “Summary” summarises this study.

Computational method

The total energy of the crystal was calculated using DFT methods (Hohenberg and Kohn 1964; Kohn and Sham 1965) implemented in the Vienna Ab initio Simulation Package, VASP (Kresse and Furthmüller 1996). The plane-wave expansion was treated using the Projected Augmented-Wave method (PAW; Blöchl 1994) with the PAW potentials generated by Kresse and Joubert (1999) and distributed with VASP. The exchange-correlation was accommodated using the PW91 generalised gradient corrected functional (Perdew 1991; Wang and Perdew 1991; Perdew and Wang 1992). This form of the generalised gradient approximation (GGA) has been demonstrated to yield the most accurate results in hydrogen-bonded systems (e.g., Tsuzuki and Lüthi 2001; Langlet et al. 2004), despite not correctly representing dispersion forces, and we have used it with great success previously to simulate a range of hydrogen-bonded substances, including epsomite (Fortes

Fig. 1 Polyhedral representation of the ambient pressure, low temperature, mirabilite structure, with the unit cell outlined in black: **a** viewed along the *a*-axis, **b** along the *b*-axis, and **c** along the *c*-axis; the labelling of the atoms is shown in **d**. The $\text{Na}(\text{H}_2\text{O})_6$ octahedra are shown in dark blue and the SO_4 tetrahedra in yellow. The interstitial H_2O molecules O10 and O11 are shown, but the H-atoms bonded to the $\text{Na}(\text{H}_2\text{O})_6$ octahedra have been omitted for clarity. A stereo version of **a** is available in the electronic supplement



et al. 2006b), several ice polymorphs (Fortes et al. 2003a; Fortes 2004), solid ammonia (Fortes et al. 2003b), and ammonia hydrates (Fortes et al. 2001, 2003c).

Convergence tests were carried out to optimise the *k*-point sampling of the Brillouin zone within the Monkhorst–Pack scheme (Monkhorst and Pack 1976), and the kinetic energy cut-off of the plane-wave basis set. It was found that gamma-point calculations combined with a kinetic energy cut-off of 800 eV yielded a total-energy convergence better than 10^{-5} eV per atom. A series of fixed volume calculations were then performed in which the ions were allowed to move according to the calculated Hellman–Feynman forces and the unit-cell shape was allowed to vary. For each volume specified the structure was relaxed via the conjugate-gradient technique in order to optimise the lattice parameters and internal coordinates.

The structural relaxations were begun using the atomic coordinates determined from neutron single-crystal diffraction analysis by Levy and Lisensky (1978), which were the most precise available at the time when the calculations were made. Since then, we have determined precise unit-cell parameters and atomic coordinates of deuterated mirabilite at 4.2 K using neutron powder diffraction (Brand et al. 2009) and neutron single-crystal diffraction (unpublished ISIS Experimental Report, RB610178). Mirabilite is a monoclinic crystal, space-group $P2_1/c$ ($Z = 4$), with unit-cell dimensions $a = 11.44214(4)$ Å, $b = 10.34276(4)$ Å,

$c = 12.75468(6)$ Å and $\beta = 107.847(1)^\circ$ at 4.2 K (Brand et al. 2009). In order to preserve continuity, we adopt in this paper the same atom labelling scheme as was used by Levy and Lisensky (1978) and Brand et al. (2009). As shown in Fig. 1 (see also Supplementary Figure S1 and S2),¹ the ambient pressure structure of mirabilite consists of edge-sharing $\text{Na}(\text{H}_2\text{O})_6$ octahedra arranged in sinuous ribbons extending along the *c*-axis, with a net stoichiometry of $\text{Na}_2(\text{H}_2\text{O})_8$. The octahedra comprise H_2O molecules, labelled as O8, O9, and O12 through O17, with the O12–O15 and O13–O14 vectors forming the shared edges. These ribbons of octahedra alternate with chains composed of sulphate tetrahedra (oxygen O4 through O7) and water molecules (labelled O10 and O11). The ribbons and chains are linked together by hydrogen bonds. The alternating ribbons of $\text{Na}_2(\text{H}_2\text{O})_8$ and SO_4 tetrahedra + H_2O thus form a flat sheet extending in the *b*–*c* plane (Fig. 1b, c). The sheets are stacked A–B–A–B along the *a*-axis, being connected by hydrogen bonds involving a combination of orientationally ordered and orientationally disordered water molecules.

The disordered H-bonds are associated with a pair of square rings of water molecules between adjacent

¹ This illustration, and a number of additional figures not included in the main text, are provided in the electronic supplement to this paper. There are also 3D representations of the mirabilite structure in the form of both stereo pairs and red-blue stereo anaglyphs; the latter require red-blue glasses in order to obtain a 3D effect.

octahedral apices, involving the molecule pairs O8/O16 (ring 1) and O9/O17 (ring 2). Each corner of the ring donates and receives one hydrogen bond from a neighbouring corner, with two possible orientations denoted ‘b’ and ‘c’ (the ‘a’ hydrogens donate bonds to sulphate oxygens outside the rings); see Supplementary Figure S3. In any one ring, all hydrogens must all be on either the ‘b’ sites or all on the ‘c’ sites. Complete orientational disorder corresponds to 50:50 occupancy of the ‘b’ and ‘c’ sites, whereas complete orientational order corresponds to either 100:0 or 0:100 occupancy of these sites. Levy and Lisensky (1978) refined this ratio, finding equal occupancy (50:50) at room temperature. Subsequently, Brand et al. (2009) confirmed this observation; they also found, however, that the occupancy of the ‘b’ orientation increased to 70% at 4.2 K, with evidence that the reduction of the disorder becomes kinetically quenched at a temperature of ~ 150 K.

Levy and Lisensky (1978) also identified disorder in the orientation of the sulphate tetrahedron at room temperature, as well as disorder in the H-bonds donated to the sulphate oxygens O4, O6, and O7. Their refined structure therefore contained additional oxygen sites, with the pairs of oxygen atoms labelled O4'/O4'', O6'/O6'', and O7'/O7''; the two sulphate orientations were related by a rotation of $\sim 30^\circ$ about the S \cdots O5 vector, with a refined value of 25:75 for the ratio of ‘prime’ to ‘double-prime’ site occupancies. In contrast, Brand et al. (2009) found no evidence for disorder associated with the sulphate tetrahedra or their related H-bonds between 4.2 and 300 K, and showed that the sulphate oxygens exclusively occupy the ‘double-prime’ sites.

Since the static DFT model cannot accommodate disorder, we fixed the sulphate tetrahedra and related H-bonds in the ‘double-prime’ orientation, shown by Brand et al. (2009) to be the experimentally preferred structure; we also fixed the relative occupancy of the ‘b’ and ‘c’ hydrogens in the square rings at 100:0, since experimental measurements had indicated that they were tending towards these values in the low temperature limit.

Using the atomic coordinates and experimental values of the cell parameters as described above, the athermal simulations were begun by relaxing the crystal structure and unit-cell parameters until a minimum energy was found with zero pressure on the unit-cell; this point corresponded to a unit-cell volume of $\sim 1470 \text{ \AA}^3$. Starting from this structure, a series of relaxations were then performed with the unit-cell volumes fixed both at successively smaller and successively higher volumes; in each case the unit-cell (subject to the constraint of fixed volume) and atomic coordinates were relaxed. With one exception (see “Possible phase transformations in mirabilite at high pressure”), the simulations were performed stepwise, with the structure from the previous simulation used as the starting structure for the next.

Results

Possible phase transformations in mirabilite at high pressure

The total energy per unit-cell was calculated as described above at a series of fixed unit-cell volumes in the range $682 < V < 1810 \text{ \AA}^3$ ($0.78 < (V/V_0)^{1/3} < 1.08$); the corresponding pressure range is $61.0 < P < -2.7$ GPa. In the electronic supplement to this paper we have provided all of the relaxed atomic structures in CIF format along with the total energies and pressures computed by VASP. The volume dependence of the total energy, $E(V)$, is shown in Fig. 2a and b. Clearly, there is a break in slope at $V \approx 1200 \text{ \AA}^3$ which is indicative of a phase transition. Figure 2b also reveals that for $\sim 1080 \text{ \AA}^3 < V < \sim 1200 \text{ \AA}^3$ the relationship between energy and volume is linear (dashed line); since $P = -(\partial E/\partial V)_T$, this region is, therefore, isobaric, indicating that the phase transition must be first-order in nature, i.e., $V(P)$ is discontinuous.

This first phase transition is more clearly seen in Fig. 2c and d, which show the behaviour of the unit-cell volume as a function of the pressure obtained from the stresses on the unit-cell simulated by VASP. The discontinuous nature of the phase transition means that the material would not exist in nature in the volume range from $\sim 1080 \text{ \AA}^3 < V < \sim 1200 \text{ \AA}^3$; the four simulations performed in this region thus correspond to transition states between low- and high-pressure phases. The transition pressure determined from the slope of the isobar on the $E(V)$ curve is 5.7 ± 0.2 GPa, in fair agreement with the mean pressure from the four VASP outputs (7.7 ± 1 GPa).

Examination of the pressure dependence of the individual unit-cell parameters, shown in Fig. 2e–h, however, strongly suggests that a further first-order phase transition occurs at a pressure of ~ 20 GPa. This transition is most clearly seen in the behaviour of the monoclinic angle, β (Fig. 2h), which takes a value of $\sim 108^\circ$ in the ambient pressure phase; at the first phase transition ($P \sim 7.7$ GPa on Fig. 2h) β falls discontinuously to $\sim 99^\circ$ and at the second transition, which occurs between ~ 18 and ~ 21 GPa, there is a further drop to $\sim 92^\circ$. A similar large discontinuous reduction (of $\sim 0.6 \text{ \AA}$) is observed in the a -axis between ~ 18 and ~ 21 GPa, following a drop of $\sim 0.75 \text{ \AA}$ at the first phase transition. The b -axis shows a discontinuous increase of about 0.05 \AA at the lower-pressure transition and 0.15 \AA at the higher one, whereas the c -axis shrinks by $\sim 1.3 \text{ \AA}$ at the first transition but shows little, if any, discontinuity at the second. The combined effect of these changes in the cell parameters is such that no obvious discontinuity in the unit-cell volume is apparent.

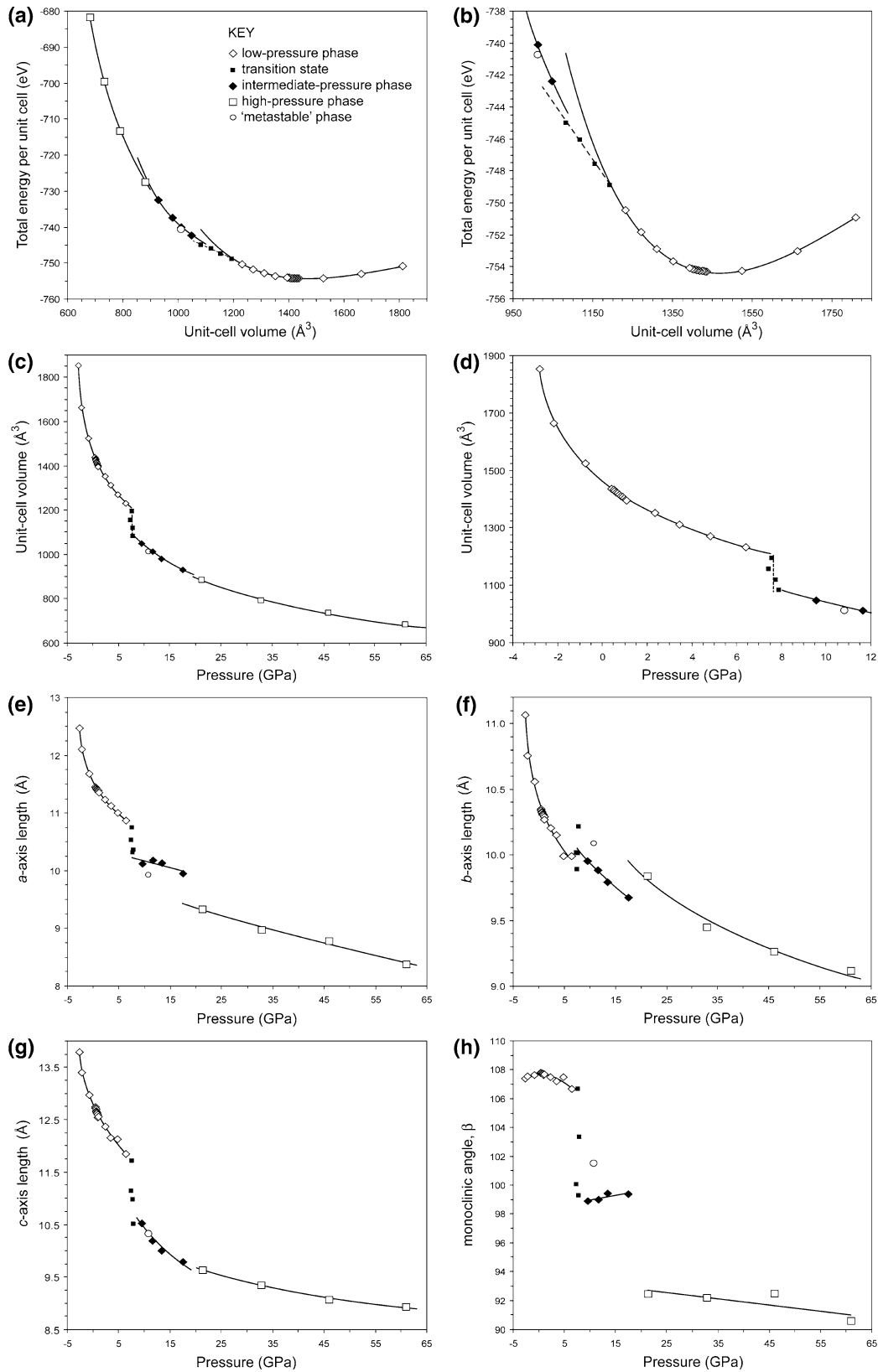


Fig. 2 Respectively, **a** and **b** report the total energy curves as a function of volume, whilst **c** and **d** report the pressure–volume curves from our ab initio calculations. **e** through **h** depict the pressure

dependence of the calculated unit-cell parameters. See text for details of the various parameterised fits shown

Analysis of the relaxed atomic coordinates using the computer programme “Endeavour” (Putz et al. 1999) indicated that the structures at ~ 13.4 GPa (intermediate phase) and 61 GPa (high-pressure phase) both retain the $P2_1/c$ symmetry of the ambient-pressure phase of mirabilite. This is unexpected, as there is no requirement for the VASP simulations to adopt any particular space group. We describe the details of the major structural re-organisations that occur at high pressure in “The high-pressure phases of mirabilite”, below.

Our calculations also suggest that there may be a second stable, or metastable, phase of mirabilite in the pressure range from 8 to 21 GPa. In Fig. 2b, it can be seen that two data points, having different energies, are shown for a unit-cell volume of 1012.8 \AA^3 . The points indicated by “filled diamonds” were obtained by relaxing the structure starting from the point at lower pressure immediately preceding it; the point indicated by the “open circle” was obtained by relaxing the structure with the next highest pressure. Examination of the SO_4 polyhedral volume of these two relaxed structures clearly shows that they have different hydrogen bond schemes (see “The SO_4 and Na coordination polyhedra” below). However, the difference in internal energy between them is very small, $\sim 4 \text{ meV atom}^{-1}$ [$1 \text{ meV atom}^{-1} = 3.57 \text{ kJ mol}^{-1}$ of $\text{Na}_2\text{SO}_4 \cdot 10\text{H}_2\text{O}$] (the enthalpy difference is $\sim 39 \text{ meV atom}^{-1}$), and, although the data point marked by a “open circle” is of marginally lower internal energy and enthalpy, all of our other VASP simulations in this volume range converged to the structure marked by the “filled diamonds”. We have included the values of the unit-cell volume and cell parameters for this second intermediate-pressure phase in Fig. 2c–h (marked by an “open circle”) and we discuss its crystal structure in “The high-pressure phases of mirabilite”. We have not, however, attempted further to investigate its stability field; the reasons for this are discussed in “Discussion”.

Although we cannot compute the energy of the high-pressure phases, in order to determine accurately their enthalpy differences, outside of their stability fields without fixing the atomic coordinates, we have made crude extrapolations (using second-order polynomials) to determine the enthalpy differences between each of the phases. At 10 GPa, we find that the intermediate-pressure phase has an enthalpy that is 35 meV atom^{-1} lower than that of the low-pressure phase. At 30 GPa, we find that the high-pressure phase has an enthalpy that is 86 meV atom^{-1} lower than that of the intermediate-pressure phase. Although these numbers may best be considered to be estimates, they do reveal the relatively small energy differences between the three phases.

The equation of state of the low-pressure phase of mirabilite

The $E(V)$ values shown in Fig. 2a and b for the low-pressure phase were fitted with an integrated form of the third-order Birch-Murnaghan equation of state (Birch 1952; referred to as BMEOS3) and an integrated form of the fourth-order logarithmic equation of state (Poirier and Tarantola 1998; referred to as LNEOS4). Both equations were fitted to $E(V)$ values in the range $1231.78 < V < 1810.61 \text{ \AA}^3$ ($0.95 < (V/V_0)^{1/3} < 1.08$). As expected, the $E(V)$ curves are flat, so the parameters obtained from these fits exhibit greater uncertainties than we have obtained in earlier work on smaller systems with higher symmetry. The fitted parameters are given in Table 1; note the agreement in all of the parameters for the low-pressure phase between BMEOS3 and LNEOS4. The value of the second pressure derivative of the incompressibility, $K_0'' = \partial^2 K_0 / \partial P^2$, for the BMEOS3 was calculated from $K_0'' = (K_0'/K_0)(7 - K_0') - (143/24)(8/3K_0)$. The $E(V)$ curve shown in Fig. 2a and b is that for the BMEOS3; the two equations of state are indistinguishable to the eye in both of these figures.

The method described above will give the most reliable equation of state parameters and the hence best estimate of $V(P)$ for the low-pressure phase of mirabilite. All of the pressure–volume curves shown in Fig. 2c and d, however, were plotted using the VASP output pressures (determined from the stresses on the unit-cell), so as to keep a common pressure scale for the full range of the simulations; the line for the BMEOS3 was, therefore, obtained by fitting the $P(V)$ values shown in the figure directly: the fitted parameters, which differ slightly from those shown in Table 1 are $V_0 = 1459.2(1) \text{ \AA}^3$, $K_0 = 23.4(3) \text{ GPa}$, and $K_0' = 5.8(1)$.

The unit-cell volume and the cell parameters corresponding to the calculated V_0 are compared with the

Table 1 Parameters obtained by least-squares fitting of the third-order Birch-Murnaghan equation of state (BMEOS3), and the fourth-order logarithmic equation of state (LNEOS4), to the $E(V)$ values for the low-pressure phase of mirabilite (unit-cell volume range: $1231.78 < V < 1810.61 \text{ \AA}^3$)

	Low pressure phase BMEOS3	Low pressure phase LNEOS4
$V_0 (\text{ \AA}^3)$	1468.6(9)	1468.4(8)
E_0 (eV per unit cell)	−754.374(5)	−754.370(5)
K_0 (GPa)	22.21(9)	21.7(3)
K_0'	5.6(1)	5.9(2)
K_0'' (GPa^{-1})	−0.37(2) ^a	0.0(2)

^a Derived from K_0 and K_0' —see text

experimental values measured at 4.2 K using neutron powder diffraction (Brand et al. 2009) in Table 2. The agreement between the DFT values and the experimental values is very good, and comparable with much of our earlier work on hydrogen-bonded solids (see “Computational method”). The difference in volume ($\Delta V/V \approx 2.2\%$) corresponds to a difference in pressure of only 0.51(1) GPa, which is small, both in absolute terms and relative to the incompressibility of the material.

Although there are, as yet, no published experimental measurements of the incompressibility of mirabilite, our results yield remarkably similar elastic moduli to those found in recent experimental and ab initio studies of epsomite (for $\text{MgSO}_4 \cdot 7\text{D}_2\text{O}$ and $\text{MgSO}_4 \cdot 7\text{H}_2\text{O}$, respectively) by Fortes et al. (2006b). For epsomite, DFT calculations in the range $-2 < P < +6$ GPa give an incompressibility of $K_0 = 23.2(2)$ GPa, with $K_0' = 5.3(2)$, in the athermal limit, whereas fits to neutron powder diffraction data in the range $0.01 < P < 0.55$ GPa at 50 K gave $K_0 = 24.9(8)$ GPa, with $K_0' = 6(3)$, and at 290 K gave $K_0 = 21.5(4)$ GPa, with $K_0' = 6(1)$. Despite major differences in the structures of epsomite and mirabilite, they clearly have similar bulk elastic properties; both as a function of pressure, and of temperature (see Brand et al. 2009).

The equations of state of the high-pressure phases of mirabilite

The instability at low pressures of the two proposed high-pressure phases of mirabilite prevents the calculation of the total energy of either of these phases in the region of their value of V_0 . It has not, therefore, been possible reliably to fit their equations of state. For example, if the $E(V)$ results for the highest-pressure phase (i.e., the four points for which $V < \sim 882 \text{ \AA}^3$ ($V/V_0)^{1/3} < 0.85$) are fitted to an

unconstrained BMEOS3, the values $V_0 = 1460 \text{ \AA}^3$, $K_0 = 7.6$ GPa, $K_0' = 6.8$ and $E_0 = -746.9$ eV are obtained (no errors are given as the number of data points is equal to the number of fitted parameters); however, if K_0' is fixed at the value obtained from the low-pressure phase ($K_0' = 5.6$), very different values of $V_0 = 1333(27) \text{ \AA}^3$, $K_0 = 14.625(8)$ GPa, and $E_0 = -744.9(9)$ eV result. For the intermediate-pressure phase, the corresponding sets of values are $V_0 = 1461 \text{ \AA}^3$, $K_0 = 14.7$ GPa, $K_0' = 4.2$ and $E_0 = -752$ eV (free refinement), and $V_0 = 1334 \text{ \AA}^3$, $K_0 = 19$ GPa and $E_0 = -748.5$ eV (with $K_0' = 5.6$). Thus, no firm conclusions can be drawn as to the values of the BMEOS3 parameters. It is interesting to note, however, that for all of the fits described above, the values of V_0 obtained were less than the value of V_0 for the low-pressure phase, as one would expect of a more densely packed structure; also, the value for V_0 that is found with K_0' fixed at 5.6 is identical to that which is obtained by applying the relative volume change at the ~ 7.7 GPa phase transition to the value of V_0 for the low- P phase.

Since reliable equation of state parameters cannot be obtained for the high-pressure phases, the lines shown in Fig. 2c and d, fitted to the BMEOS3 with K_0' fixed at the value for the low-pressure phase ($K_0' \equiv 5.6$), should be considered as merely providing a method of smoothing the data for use in our later analysis (see “Derivation of the elastic strain tensor of mirabilite”).

Derivation of the elastic strain tensor of mirabilite

In the first instance, the unit-cell parameters of the low-pressure phase of mirabilite (Fig. 2e–h) were also fitted with third-order Birch–Murnaghan expressions in order to obtain information about the axial incompressibilities. Referred to orthogonal axes, the zero-pressure axial incompressibilities

Table 2 Comparison of the unit-cell dimensions and axial ratios of the ambient-pressure phase of mirabilite obtained computationally with the experimental values for the deuterated isotopomer at 4.2 K (Brand et al. 2009)

	Experimental Neutron powder diffraction $\text{Na}_2\text{SO}_4 \cdot 10\text{D}_2\text{O}$ at 4.2 K		Computational DFT calculations $\text{Na}_2\text{SO}_4 \cdot 10\text{H}_2\text{O}$ at 0 K	Difference (%) $\frac{X_{\text{calc}} - X_{\text{obs}}}{X_{\text{obs}}} \times 100$
V (\AA^3)	1436.794(8)	V_0 (\AA^3)	1468.6(9)	2.21(6)
a (\AA)	11.44214(4)	a_0 (\AA)	11.539(2)	0.85(3)
b (\AA)	10.34276(4)	b_0 (\AA)	10.415(8)	0.70(8)
c (\AA)	12.75468(6)	c_0 (\AA)	12.828(11)	0.57(8)
β ($^\circ$)	107.847(1)	β_0 ($^\circ$)	107.74(3)	-0.10(3)
b/a	0.903918(5)	b_0/a_0	0.9026(7)	-0.14(8)
c/a	1.114711(7)	c_0/a_0	1.1120(10)	-0.27(9)
b/c	0.810899(5)	b_0/c_0	0.8119(9)	0.13(11)

The computational V_0 is from the BMEOS3 fit to $E(V)$ (see Table 1), and the cell parameters are from independent BMEOS3 fits to the relaxed unit-cell dimensions as a function of the EoS-derived pressure scale (axial K_0 and K_0' from these fits are cited in the text), with β taken from a third-order polynomial fit; note that the computational unit-cell dimensions give $V_0 = 1468(2) \text{ \AA}^3$

and their first pressure derivatives were found to be, $K_{0asin\beta} = 76(1)$ GPa, $K'_{0asin\beta} = 17.9(5)$, $K_{0b} = 92(4)$ GPa, $K'_{0b} = 21(2)$, and $K_{0c} = 55(2)$ GPa, $K'_{0c} = 10.4(9)$. As a check, we computed the zero-pressure bulk modulus, $K_0 = [(K_{0asin\beta})^{-1} + (K_{0b})^{-1} + (K_{0c})^{-1}]^{-1} = 23.0(4)$ GPa, which is in fair agreement with the value found earlier. It is surprising to find that the most compressible direction is along the c -axis; as discussed in “[The SO₄ and Na coordination polyhedra](#)”, this is most likely due to the softness of the NaO₆ octahedra rather than any propensity to accommodate compression by folding at the shared hinges.

This simple analysis of the elastic anisotropy does not allow us to understand the changes in elastic behaviour brought about by the significant structural changes as a function of pressure. We have therefore used the relaxed unit-cell dimensions (Fig. 2e–h) to determine the coefficients of the elastic strain tensor as a function of pressure using the method described by Hazen et al. (2000). The eigenvalues and eigenvectors of the strain tensor were obtained by matrix decomposition, yielding the magnitudes and orientations of the principal axes of the strain ellipsoid, ε_1 , ε_2 , and ε_3 . The magnitudes of the principal axes are strains per unit stress, and are effectively axial compressibilities; their sum is the (negative) bulk compressibility. The ellipsoid is constrained by the symmetry of the crystal to rotate only about the two-fold axis; we have chosen to adopt the convention that the principal strain axis ε_2 is parallel to the b -axis of the crystal.

Strains were calculated using the relaxed unit-cell dimensions output by VASP and also using equations of state fitted to that same output. For the low-pressure unit-cell, it was possible to fit BMEOS3 expressions to the a -, b -, and c -axes, together with a third-order polynomial to represent the behaviour of the monoclinic angle, β . Due to the limited number of high-pressure points, we fitted Murnaghan integrated linear equations of state (MILEOS), i.e.,

$$X = X_0 \left(\frac{K_0}{K_0 + K'_0 P} \right)^{1/K'_0}$$

to the unit-cell axes of the two high-pressure phases, and linear expressions for the β -angle (these are, respectively, the solid, dashed, and dotted lines in Fig. 2e–h).

The lines in Fig. 3 are the strains obtained from the various EoS fits; only for the volume do we show strains computed from the individual calculations, since the strains computed from the ‘raw’ unit-cell dimensions are very noisy. Also shown in Fig. 3d is the angle between ε_3 and the crystallographic c -axis.

Bearing in mind that the strain ellipsoid for the high-pressure phase is quite sensitive to the uncertainties in the EoS fitting, Fig. 3 reveals significant discontinuities in all three principal axes. In each of the axes the three separate phases, low, intermediate and high pressures are clearly

visible, with a smaller offset at the transition from intermediate to high pressure than for that from the low to intermediate pressure phases.

The orientation of the strain ellipsoid in the a - c plane changes considerably as a function of pressure (Fig. 3d). At $P = 0$, ε_1 is closely aligned with the crystallographic a -axis, and ε_3 is consequently tilted $\sim 10^\circ$ from the c -axis towards the +ve a -axis. Under compression, the angle between ε_3 and the c -axis shrinks, passing through zero at ~ 1.2 GPa, and continuing to rotate through a further 23° with increasing pressure. At the transition, the ellipsoid ‘slips’ back, bringing ε_3 to near coincidence with the c -axis before rotating through $\sim 10^\circ$ until the transition to the high pressure structure, at which point the rate of rotation increases and the angle rapidly changes as ε_3 saturates at about 20° from the a -axis.

We have been unable to identify any single mechanism which might explain the rotation of the ellipsoid through $\sim 35^\circ$ from 0 to 7.5 GPa. There are very small rotations with respect to the crystallographic axes of various structural units (such as the SO₄ tetrahedra and the square H-bonded rings), but these amount to little more than $\sim 3^\circ$. Furthermore, there is no evidence of rotation due to kinking of the Na–O chains along the shared hinges. The stiffening roughly along the c -axis is probably due to the expansion and stiffening of the Na–O polyhedra (see “[The SO₄ and Na coordination polyhedra](#)”) whereas the softening roughly along the a -axis is likely due to a reduction in interlayer hydrogen bonding.

In the following section, we report the agreement between the simulated structure at zero-pressure and the experimentally observed structure, before going on to describe the pressure-dependent changes.

The zero-pressure, zero-temperature structure

Tables 3 and 4 report comparisons of our calculated bond lengths² at zero-pressure in the athermal limit with the experimentally observed bond lengths in mirabilite at atmospheric pressure and 4.2 K (Brand et al. 2009). It should be noted, however, that the difficulty of the neutron powder refinement (with respect to the large number of refined variables) required heavy bond-length restraints on S–O and O–D bond lengths and angles (see Brand et al. 2009 for a full discussion of the refinement process) which will bias the experimental values. Table 3 shows that both the calculated S–O bond lengths, and the Na–O bond lengths (with two exceptions), are systematically 2–3% longer than is observed experimentally. This means that the zero-pressure volume of the SO₄ tetrahedron, $1.7358(5) \text{ \AA}^3$,

² Atomic coordinates provided in the electronic supplement.

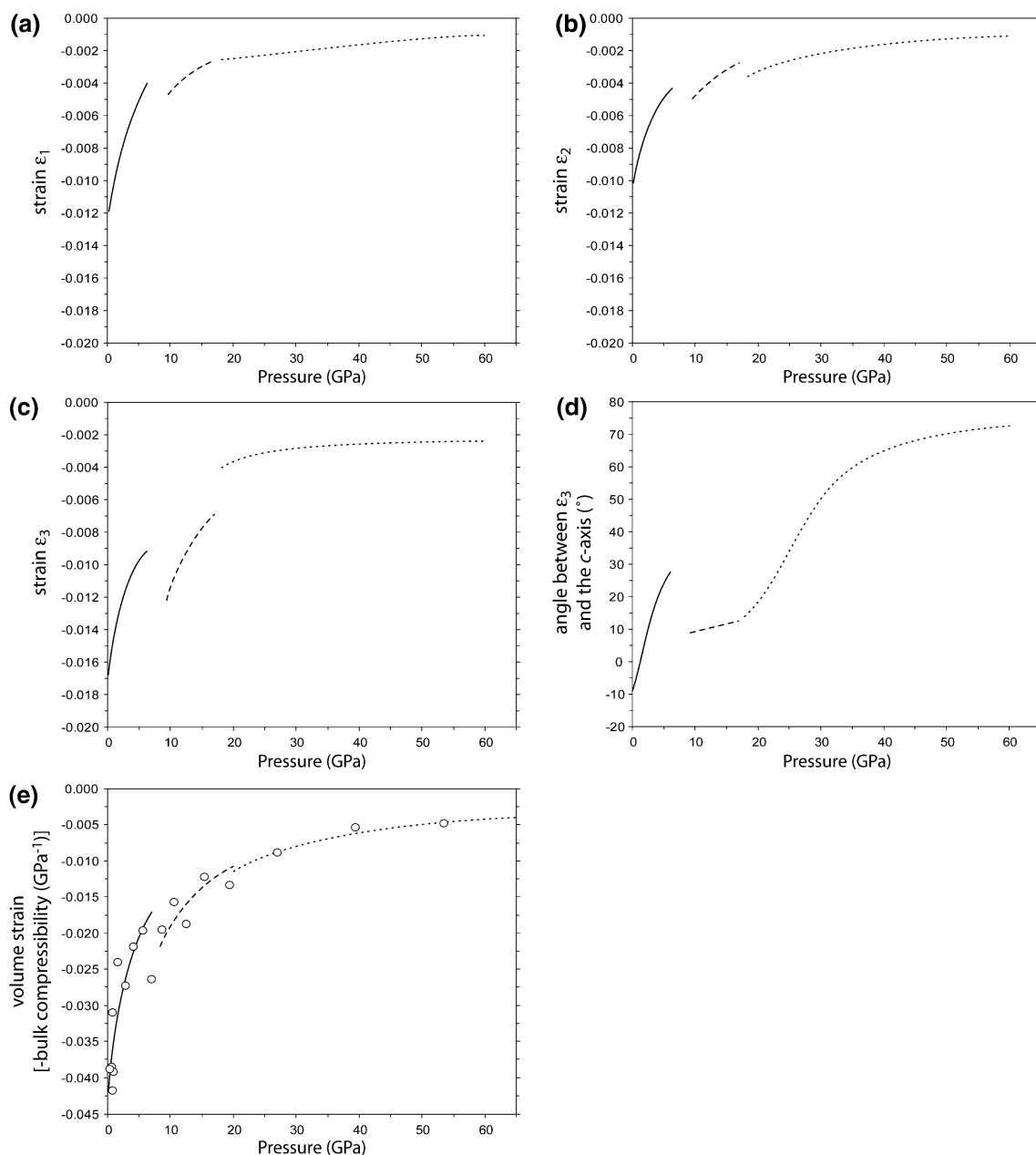


Fig. 3 a–c show the magnitudes of the principal axes of the strain tensor, ϵ_1 , ϵ_2 and ϵ_3 as a function of pressure; the angle between ϵ_3 and the crystallographic c -axis is shown in **d** and the volume

compressibility is shown in **e**. In **d**, angles $> 0^\circ$ correspond to the vector ϵ_3 lying between $[\bar{1}00]$ and $[001]$, i.e., the angle is measured clockwise when viewed along the direction $[0\bar{1}0]$

is 7.0% greater than the experimental value. Similarly, the volumes of the Na2 and Na3 octahedra, $21.17(7) \text{ \AA}^3$ and $22.0(2) \text{ \AA}^3$, respectively, are 6.9 and 10.5% greater than the equivalent experimental volumes. Indeed, of the 31.8 \AA^3 difference between the experimental and DFT unit-cell volume, fully 43% is due to over-inflation of the NaO_6 octahedra, and just 1.4% is due to over-inflation of the SO_4 tetrahedra.

In Table 4 the experimental and computational bond distances involving the hydrogen atoms are compared; it

can be seen that, with the marked exception of the hydrogen bonding in the square rings, the agreement between calculation and experiment is excellent. Covalent O–H bonds are generally longer by approximately 0.5%; given the restraints employed in the neutron powder refinement, we do not consider this difference to be significant. The calculated hydrogen bonds ($\text{H}\cdots\text{O}$) are slightly stronger, resulting in bond lengths which, for the most part, are shorter by 0.5–2% than is observed experimentally. Nonetheless, the correlation between the

Table 3 Comparison of the S–O and Na–O bond lengths (in Å) of the ambient-pressure phase of mirabilite obtained computationally with the experimental values from the deuterated isotopomer at 4.2 K (Brand et al. 2009)

	Experimental neutron powder diffraction Na ₂ SO ₄ ·10D ₂ O at 4.2 K	Computational DFT calculations Na ₂ SO ₄ ·10H ₂ O at 0 K (athermal) and zero-pressure	Difference (%) $\frac{X_{\text{calc}} - X_{\text{obs}}}{X_{\text{obs}}} \times 100$
S–O4	1.466(2)*	1.5060(2)	2.7(1)
S–O5	1.467(2)*	1.5015(2)	2.4(1)
S–O6	1.469(2)*	1.5017(2)	2.2(1)
S–O7	1.468(2)*	1.4952(3)	1.9(1)
Na2–O12	2.433(9)	2.479(3)	1.9(4)
Na2–O13	2.409(9)	2.470(2)	2.5(4)
Na2–O14	2.403(9)	2.393(2)	–0.4(4)
Na2–O15	2.378(9)	2.414(3)	1.5(4)
Na2–O16	2.429(9)	2.513(2)	3.5(4)
Na2–O17	2.390(9)	2.461(2)	3.0(4)
Na3–O8	2.386(8)	2.437(1)	2.1(3)
Na3–O9	2.369(8)	2.422(1)	2.2(3)
Na3–O12	2.459(8)	2.466(1)	0.3(3)
Na3–O13	2.409(8)	2.485(2)	3.2(3)
Na3–O14	2.354(8)	2.420(2)	2.8(4)
Na3–O15	2.418(8)	2.481(2)	2.6(3)

* Values were restrained during refinement—see Brand et al. (2009) for details

calculated and experimental H··O bond lengths is high (excluding the square ring H··O bonds, the correlation coefficient = 0.935), showing that the pattern of hydrogen-bonding has been faithfully reproduced in spite of the lack of van der Waals contributions in the DFT approximation. This is supported by an examination of the hydrogen-bond angles ($\angle\text{O–H}\cdots\text{O}$), reported in Table 4; with the exception of two outliers, both of which are involved in the square rings, and which differ by >5%, the correlation coefficient between the calculated and observed bond angles is 0.869. All but three of the H-bonds in the DFT structure are straighter than in the observed structure at 4.2 K (i.e., bond angles closer to 180°), with the differences in angle in the range 0–3.3%. However, this difference in the bending of the H-bonds is not responsible for the remaining 55% of the volume difference not already accommodated by over-inflated SO₄ and NaO₆ polyhedra. In fact, the straightening of the bonds is offset by the shortening of the H··O contact, resulting in calculated O–O distances which differ by barely 0.5% from experiment.

The major difference between experiment and DFT calculation is found in the O–H and H··O bonds involved in the square rings. These O–H bonds are roughly 1.5% longer than any of the other O–H bonds in the DFT structure, and the H··O bonds are significantly shorter. The difference in H··O bond length between experiment and calculation is also large (average 4.5%). It is our opinion that these differences are due to the elimination of the partially ordered ‘c’ hydrogen sites in the structure; the orientational disorder of the O8/O16 and O9/O17 water molecules certainly contributes additional volume in the

form of Bjerrum defects, and these are wholly lacking in the simulated structure. This difference between the observed and simulated structure also affects the behaviour under pressure, as described in the following section.

The pressure dependence of the structural parameters

In the majority of crystal structures, the application of pressure results in shortening of interatomic and intermolecular bonds. However, in hydrogen-bonded crystals it is typical to observe lengthening of O–H bonds under pressure as the electron density in the hydrogen bond increases. In water ice this results in the hydrogen atoms moving to a position midway between neighbouring oxygens at pressures of 60–70 GPa; this is the so-called bond-symmetric phase ice X. In many other hydrogen-bonded crystals, however, proton transfer may occur, resulting in a partially or wholly ionic structure (e.g., Fortes et al. 2001; Pickard and Needs 2008). It is therefore of interest to establish the pressure dependence of the various bond lengths in mirabilite. The atomic coordinates for all of the high-pressure structures are provided in the electronic supplement.

The SO₄ and Na coordination polyhedra

We have fitted third-order Birch-Murnaghan expressions to the calculated volumes of the polyhedral units in the mirabilite structure as a function of pressure; these fits provide the zero-pressure volumes reported in “The zero-pressure, zero-temperature structure”, and the polyhedral bulk moduli. All polyhedral volumes were computed using

Table 4 Comparison of the O–H(D) and H(D)–O bond lengths (in Å) of the ambient-pressure phase of mirabilite obtained computationally with the experimental values of the deuterated isotopomer at 4.2 K (Brand et al. 2009)

	Covalent bond lengths, O–H(D)			Hydrogen bond lengths, H(D)···O			Hydrogen bond angles ∠O–H(D)···O		
	Experiment O–D	Calculation O–H	Difference (%) $\frac{X_{\text{calc}} - X_{\text{obs}}}{X_{\text{obs}}} \times 100$	Experiment D···O	Calculation H···O	Difference (%) $\frac{X_{\text{calc}} - X_{\text{obs}}}{X_{\text{obs}}} \times 100$	Experiment ∠O–D···O	Calculation ∠O–H···O	Difference (%) $\frac{X_{\text{calc}} - X_{\text{obs}}}{X_{\text{obs}}} \times 100$
O8–H8b···O16	0.9897(21)	1.0048(1) (+)	1.5(2)	1.842(6)	1.705(1)	–7.4(3)	157.7(5)	171.0(2)	8.4(3)
O9–H9b···O17	0.9899(21)	1.0034(2) (+)	1.4(2)	1.786(6)	1.711(3)	–4.2(4)	168.8(6)	170.6(3)	1.1(4)
O16–H16b···O8	0.9886(21)	1.0005(2) (+)	0.6(2)	1.766(6)	1.726(3)	–2.3(4)	171.6(5)	160.8(2)	–6.3(3)
O17–H17b···O9	0.9924(21)	1.0072(1) (+)	0.2(2)	1.753(6)	1.678(1)	–4.3(3)	167.5(5)	169.9(2)	1.4(3)
O12–H12a···O10	0.9845(21)	0.9913(2)	0.7(2)	1.863(6)	1.835(2)	–1.5(3)	177.7(5)	178.9(2)	0.7(3)
O13–H13a···O11	0.9842(21)	0.9892(2)	0.5(2)	1.866(6)	1.880(3)	0.8(4)	177.0(5)	178.3(2)	0.7(3)
O14–H14a···O10	0.9876(21)	0.9937(2)	0.6(2)	1.802(6)	1.782(4)	–1.1(4)	168.1(4)	171.7(2)	2.1(3)
O15–H15b···O11	0.9865(21)	0.9939(2)	0.8(2)	1.829(6)	1.788(5)	–2.2(4)	166.5(4)	172.5(3)	3.6(3)
O10–H10a···O5	0.9864(21)	0.9903(2)	0.4(2)	1.839(5)	1.857(8)	–1.0(5)	170.4(4)	170.9(2)	0.3(3)
O10–H10b···O4	0.9836(21)	0.9885(2)	0.5(2)	1.849(5)	1.837(2)	–0.6(3)	170.2(4)	170.3(2)	0.1(3)
O11–H11a···O4	0.9856(21)	0.9887(2)	0.3(2)	1.848(5)	1.859(5)	0.6(4)	174.8(5)	176.8(2)	1.1(3)
O11–H11b···O6	0.9860(21)	0.9901(2)	0.4(2)	1.855(5)	1.862(6)	0.4(4)	165.9(4)	169.5(3)	2.2(3)
O9–H9a···O4	0.9851(21)	0.9893(2) (–)	0.4(2)	1.764(6)	1.753(5)*	–0.6(4)	174.8(4)	175.2(3)	0.2(3)
O8–H8a···O5	0.9845(21)	0.9876(2) (–)	0.3(2)	1.811(6)	1.804(6)	–0.4(5)	165.7(4)	166.7(1)	0.6(2)
O12–H12b···O5	0.9813(20)	0.9824(2) (–)	0.1(2)	1.946(5)	1.977(3)	1.6(3)	170.7(5)	170.7(3)	0.0(3)
O13–H13b···O6	0.9869(20)	0.9832(2) (–)	–0.4(2)	1.938(5)	1.937(5)	–0.1(4)	171.6(4)	172.9(1)	0.8(2)
O17–H17a···O6	0.9847(21)	0.9863(2) (–)	0.2(2)	1.941(6)	1.898(2)	–2.2(3)	170.5(5)	171.7(3)	0.7(3)
O14–H14b···O7	0.9901(21)	0.9862(2) (–)	–0.4(2)	1.828(5)	1.816(1)	–0.7(3)	168.3(5)	171.49(4)	1.9(3)
O15–H15a···O7	0.9892(21)	0.9849(2) (–)	–0.4(2)	1.825(5)	1.808(3)*	–1.0(3)	167.4(4)	167.2(1)	–0.1(2)
O16–H16a···O7	0.9850(21)	0.9855(2) (–)	0.0(2)	1.821(5)	1.828(7)	0.4(5)	165.4(5)	161.3(4)	–2.5(4)

Note that these have been grouped as follows; hydrogen bonds involved in forming the square rings in the low-*P* phase (first four rows); hydrogen bonds donated to interstitial waters (rows 5–8); hydrogen bonds donated by interstitial waters (rows 9–12); other hydrogen bonds, Na-coordinated waters donating to sulfate oxygens. In column 3, the symbol (+) indicates that the bond increases in length as a function of pressure, (–) denotes a decrease in length with pressure, and the absence of a symbol indicates a negligible change in length with pressure (see text for further discussion). In column 6, asterisks mark the two hydrogen bonds which are exceptionally stiff in comparison to all the others (see text)

the programme DRAWxtl (Finger et al. 2007). The SO₄ tetrahedron is comparatively stiff, with $V_0 = 1.7358(5) \text{ \AA}^3$, $K_0 = 170(5) \text{ GPa}$, and $K_0' = 17(3)$, in the low-pressure phase. When these values are compared to the DFT equation of state of the SO₄ tetrahedron in epsomite (Fortes et al. 2006b), which has $V_0 = 1.7374(7) \text{ \AA}^3$, $K_0 = 244(11) \text{ GPa}$, and $K_0' = 25(8)$, it is apparent that the values of V_0 are in very close agreement; the only significant dissimilarity is in the stiffness, which we attribute to the disparity in electron density around the apical oxygens caused by the difference in the number of accepted hydrogen bonds—twelve in mirabilite and eight in epsomite. Thus, although the rate at which the SO₄ tetrahedron stiffens is structure dependent, the volume that it occupies at zero-pressure volume is insensitive to the crystal structure. This hypothesis is supported by the observation that when the number of hydrogen bonds donated to the SO₄ tetrahedron in mirabilite drops to ten following the first high-pressure phase transition at $\sim 7.7 \text{ GPa}$, the volume of the SO₄ tetrahedron increases so that it is similar to that predicted by the equation of state of the epsomite SO₄ tetrahedron (Fig. 6a). Moreover, at pressures above the second phase

transition at $\sim 19 \text{ GPa}$, when the number of H-bonds donated to the mirabilite SO₄ tetrahedron drops to six there is a further expansion and stiffening ($K_0 > 550 \text{ GPa}$, with V_0 fixed at 1.736 \AA^3 , see above), as shown in Fig. 4b.

Figure 4 also reveals very clearly the difference in crystal structure between the two polymorphs found in the pressure range from ~ 7.7 to $\sim 19 \text{ GPa}$. The majority of the data in this region correspond to structures with ten hydrogen bonds donated to the SO₄ tetrahedron, whereas the second polymorph, represented in Fig. 2 by the single data point (the open circle), has a structure in which eleven hydrogen bonds are donated to the SO₄ tetrahedron.

Similar changes are observed in the NaO₆ octahedra under compression. In the low-pressure phase, the Na2 octahedron has BMEOS3 parameters $V_0 = 21.17(7) \text{ \AA}^3$, $K_0 = 19(2) \text{ GPa}$ and $K_0' = 5.6(9)$, while the Na3 octahedron has BMEOS3 parameters $V_0 = 22.0(2) \text{ \AA}^3$, $K_0 = 14(3) \text{ GPa}$ and $K_0' = 4.4(11)$. The NaO₆ octahedra are roughly an order of magnitude softer than the SO₄ tetrahedra and indeed are more compressible than the bulk crystal. The only literature reporting the polyhedral bulk modulus of NaO₆ octahedra pertains to the sodium-bearing

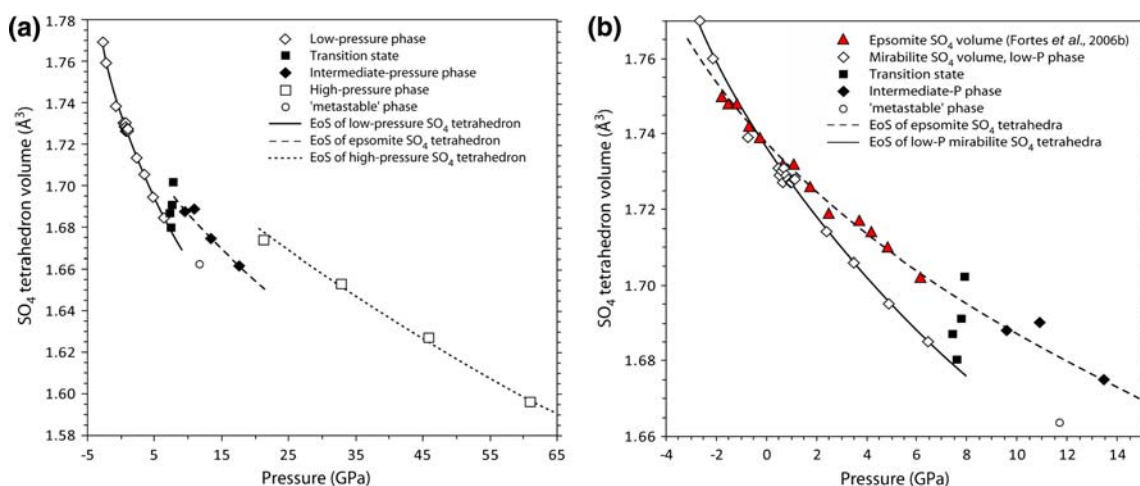


Fig. 4 Ab initio sulphate tetrahedron volumes as a function of pressure for epsomite (Fortes et al. 2006b), and for mirabilite (this work). The solid line is a BMEOS3 fit to the SO₄ volumes in mirabilite for the low-pressure phase, and the dashed line is a

BMEOS3 fit to the SO₄ volumes in epsomite. The dotted line at higher pressure is a BMEOS3 fit to the four values above 20 GPa with V₀ fixed equal to 1.736 Å³ (see text for details)

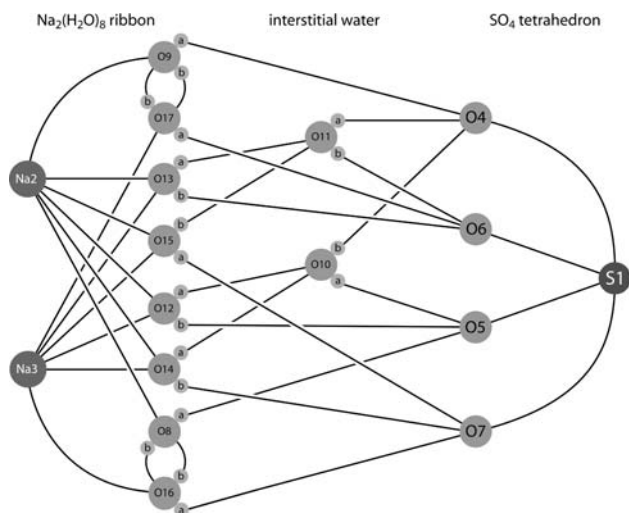


Fig. 5 Connectivity map illustrating the relationship between structural elements in mirabilite at zero pressure; the hydrogen bond structure depicted corresponds to the full ordering of the ‘b’ sites attached to O9/O17 and O8/O16 (see also Supplementary Figure S3). Note that this map differs slightly from that depicted in Brand et al. (2009) in order to aid comparison with subsequent maps

clinopyroxenes aegirine and jadeite, where Na⁺ is coordinated by O²⁻, rather than by neutral H₂O; these have bulk moduli of ~67 and ~70 GPa, respectively (McCarthy 2007). Interestingly, in both of these minerals, the NaO₆ octahedra are also more compressible than the bulk crystal. However, by applying the theoretical relationship of Hazen and Finger (1979), we can make an estimate of the expected incompressibilities of the NaO₆ octahedra in mirabilite from the incompressibility of the MgO₆ octahedron in epsomite, which has a value of 52(2) GPa (Fortes et al. 2006b). The ratio of the bulk moduli is simply:

$$\frac{K_{\text{Na-O}}^{\text{mirabilite}}}{K_{\text{Mg-O}}^{\text{epsomite}}} = \frac{z_{\text{Na}}}{z_{\text{Mg}}} \cdot \frac{\langle \text{Mg-O} \rangle^3}{\langle \text{Na-O} \rangle^3}$$

where z_{Na} and z_{Mg} are the formal charges on the ions (+1 and +2, respectively), and ⟨Mg–O⟩ and ⟨Na–O⟩ are the average cation–anion distances in the polyhedra (2.090 and 2.454 Å, respectively). Hazen and Finger (1979) observe that the connectivity (i.e., isolated polyhedra vs. edge-sharing or face-sharing) does not affect the validity of the relationship. Using the equation above we find that the ratio of the bulk moduli is 0.309 and therefore the predicted incompressibility of the NaO₆ octahedra in mirabilite in the low-pressure phase is 16 GPa, in excellent agreement with the ab initio calculations. Analysis of the angles between opposing plane faces on the shared hinges reveals that these are extremely stiff, permitting no more than 0.3° GPa⁻¹ of tilt between adjacent octahedra in the low-P phase. Hence, in this phase, it is solely the compression of these octahedra that is responsible for the softness of the c-axis rather than tilting along shared hinges.

As described below, the transitions to the high-pressure phases are characterised primarily by a change in sodium coordination, which finally changes the NaO₆ octahedra into NaO₇ decahedra, whereupon the volume of these polyhedra increases from ~17 to ~35 Å³, with a consequent stiffening of the polyhedral bulk modulus (see “The high-pressure phases of mirabilite”).

The behaviour of bonds involving H atoms in the low-pressure phase

In the low-pressure phase, the O–H bonds respond to pressure in one of three ways. One group of bonds shrinks at a

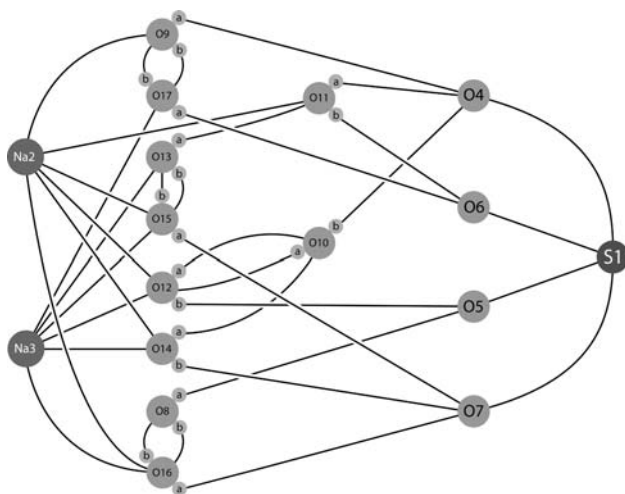


Fig. 6 Connectivity map illustrating the relationship between structural elements in mirabilite in the intermediate phase at a pressure of 13.4 GPa. The connectivity in the second intermediate phase, represented by the “open circle” in Fig. 2, differs only in that there is an additional H-bond from O6–H13b

rate of $-1 \times 10^{-3} \text{ \AA GPa}^{-1}$; a second group expands at a rate of $1.5\text{--}2.01 \times 10^{-3} \text{ \AA GPa}^{-1}$; and a third group exhibits a negligible change in length ($10^{-4}\text{--}10^{-5} \text{ \AA GPa}^{-1}$). In Table 4, the first group are marked (–), the second are marked (+), and the third have no extra mark. It is very clear that all of the O–H bonds which increase in length occur in the square rings (O8/16 and O9/17), and all of the O–H bonds which are insensitive to pressure either donate H-bonds to interstitial waters, or form the interstitial waters (O10 and O11). The remainder of the H-bonds shrink under pressure, which is the opposite response to that observed in, for example, water ice. The O–H bonds in the square rings are notable for being longer than all of the other O–H bonds at zero-pressure and thus their donation of much shorter (and hence stronger) hydrogen bonds.

The pressure response of the hydrogen bonds themselves is quite interesting. We have fitted MILEOS expressions to obtain their linear incompressibility ($K = -x \cdot dP/dx$), and find that there is no correlation between bond length and bond stiffness. Two H-bonds (marked by asterisks in Table 4) stand out as being exceptionally stiff ($K_0 = 125\text{--}130 \text{ GPa}$) compared to the average ($K_0 = 35 \pm 12 \text{ GPa}$ excluding these two outliers), but it is not at all obvious why this should be so. The weakest H-bonds, with linear incompressibilities of 17–30 GPa, are those donated by the interstitial waters O10 and O11 to the sulphate oxygens O4, O5, and O6.

The high-pressure phases of mirabilite

As described previously, our calculations reveal that mirabilite experiences two-first-order phase transformation

at ~ 7.5 and $\sim 20 \text{ GPa}$. In order to appreciate the complex structural changes which occur, we have created maps illustrating the molecular connectivity for (1) the low pressure phase—Fig. 5; (2) the intermediate phase—Fig. 6; and (3) the high pressure phase—Figs. 7 and 8.

The most notable structural changes at high pressure involve the ribbons of Na ions and their coordination polyhedra of water molecules. In the high-pressure phases these ribbons become more buckled; this buckling changes firstly the molecules that lie at the vertices of the coordination polyhedron of Na2 and then, at higher pressure, the number of vertices in both of the polyhedra. The changes that occur across the 7.5 GPa discontinuity are as follows. Although in both the low-pressure and intermediate pressure states the sodium atoms are coordinated to six oxygens in an octahedral arrangement, in the intermediate-pressure phase: the water molecule containing O16 now forms one of the vertices of the polyhedron around Na2 as well as that around Na3; the interstitial water molecule containing O11 moves closer to Na2 and forms another of the octahedral vertices; the water molecules containing O8 and O13 move further away (in the second intermediate phase—that represented by a single point on Fig. 2—the same changes in the coordination of Na2 occur). In the high-pressure phase, above $\sim 20 \text{ GPa}$, both of the sodium atoms are coordinated to seven oxygen atoms in a decahedral arrangement; Na2 loses the molecules containing O11 and O16, replacing them with those containing O8 and O13 (as in the low-pressure phase), and, in addition, gains the water molecule containing O17; Na3 gains the water molecule containing O8. In the low- and intermediate-pressure phases the octahedra are edge-sharing, but at high pressures the polyhedra have a pair of shared faces, defined by planes joining O12–O15–O17 and O8–O13–O14.

To accommodate the coordination change around the sodium atoms, there must be a major reorganisation of the hydrogen-bond framework which forms the ‘scaffolding’ within which sits the $\text{Na}_2(\text{H}_2\text{O})_8$ ribbons and the SO_4 tetrahedra. In the intermediate-pressure phases, the square rings involving O8 and O16, and O9 and O17 are preserved, but the transition to the high-pressure phase results in the destruction of the square ring involving O8 and O16, although the ring comprised of O9 and O17 is preserved. Despite the loss of the O8/O16 ring, these molecules do form a new square ring (without the twofold rotation axis, clearly) involving O14 and the interstitial water molecule O10 (Fig. 7). Another new square ring is also formed from a Na-coordinated water (O12) and an interstitial water (O10), with an axis of twofold rotational symmetry passing through its centre. Both O8/O16 and O9/O17 each swap one of their hydrogen atoms (as marked on Fig. 7), which is in agreement with the observation that these are the only O–H bonds that increase in length as a function of pressure.

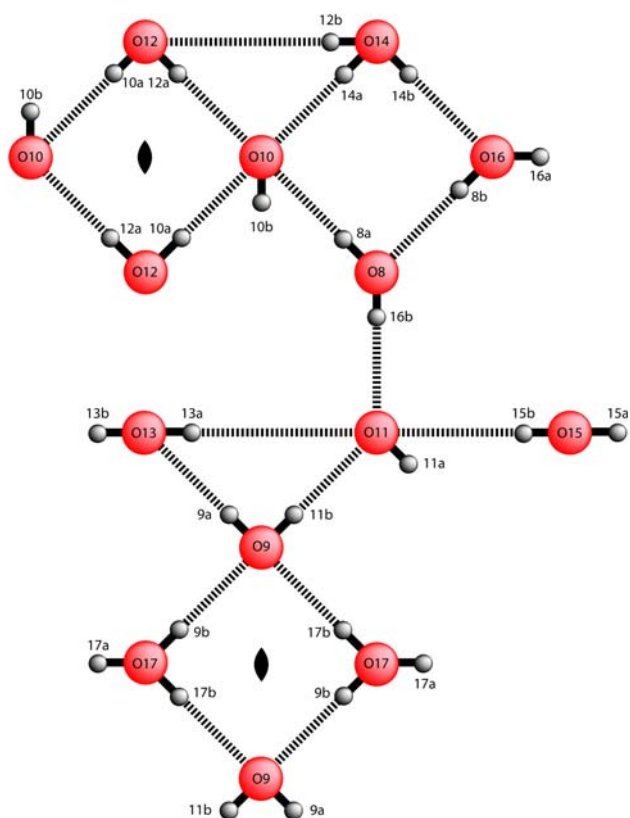


Fig. 9 Schematic illustrating the connectivity, forming a series of three- and four-sided rings, in the high-pressure hydrogen-bond network of mirabilite at 61 GPa. This format reveals some of the spatial relationships which are difficult to detect in structure maps such as Fig. 8. Notice that hydronium O14 is directly H-bonded to the hydroxide ion O10 whereas hydronium O17 is not directly bonded to hydroxide O11

very weak H-bond donor (e.g., Botti et al. 2004); both of the OH^- ions in the high-pressure phase of mirabilite accept four H-bonds.

At the very highest pressures, we also observe a gradual reduction in the distance between Na2 and the sulphate

oxygen O6, and between Na3 and O11. Although the coordination polyhedra surrounding the sodium cations are characterised by Na–O bond lengths of $\sim 2.1\text{--}2.2$ Å, the O6 and O11 oxygens are approaching to within 2.3–2.4 Å of their respective Na cations. Arguably, these atoms may be considered to be coordinated to the Na cation at this (and higher) pressures, forming face-sharing NaO_8 trikaidecahedra. Interestingly, direct coordination of the Na cation by sulphate oxygens is observed in the newly discovered octahydrate of sodium sulphate, which is only stable under high-pressure (Oswald et al. 2009).

Discussion

In the absence of any published high-pressure structural data for mirabilite, we can instead compare the elastic response of the structure to pressure with the elastic response of the structure to temperature, which has been measured for the perdeuterated isotopologue (Brand et al. 2009). In the latter experimental study, we were able to obtain an estimate of the bulk modulus by applying a Grüneisen approximation to the thermal expansion, with the necessary internal energy contribution calculated (cf., Wallace 1998) from the measured specific heat capacity (Brodale and Giauque 1958; Ruben et al. 1961). This procedure gave us a value for the ratio of the bulk modulus to the Grüneisen parameter, $K_0/\gamma = 29(1)$ GPa; since γ is typically of order 1, then we may reasonably predict that $K_0 \approx 29$ GPa, in tolerable agreement with the calculations.

In our analysis of the anisotropic thermal expansion (Brand et al. 2009) we found that the *b*-axis corresponds to the direction of smallest thermal expansion, whereas the principal axis of the thermal expansion tensor closest to the *c*-axis has the largest thermal expansivity and that closest to the *a*-axis an intermediate value. This agrees with our

Table 5 Geometry of the ionic species in the high-pressure phase of mirabilite at 61 GPa, and their donated hydrogen bonds

O14 hydronium geometry						
O14–H14a	1.0567 Å	H14a...O10	1.2775 Å	$\angle\text{H14a-O14-H14b}$	96.30°	
O14–H14b	1.0815 Å	H14b...O16	1.2849 Å	$\angle\text{H14a-O14-H12a}$	109.49°	
O14–H12a	1.0543 Å	H12a...O12	1.3136 Å	$\angle\text{H14b-O14-H12a}$	93.47°	
O17 hydronium geometry						
O17–H17a	1.0256 Å	H17a...O7	1.3164 Å	$\angle\text{H17a-O17-H17b}$	103.44°	
O17–H17b	1.0571 Å	H17b...O9	1.3934 Å	$\angle\text{H17a-O17-H9b}$	101.20°	
O17–H9b	1.0432 Å	H9b...O9	1.3712 Å	$\angle\text{H17b-O17-H9b}$	105.01°	
O10 hydroxide geometry						
O10–H10b	0.9733 Å	H10b...O4	1.4744 Å	$\angle\text{O10-H10b-O4}$	141.19°	
O11 hydroxide geometry						
O11–H11a	0.9763 Å	H11a...O5	1.6397 Å	$\angle\text{O11-H11a-O5}$	138.63°	

present DFT results inasmuch as the least compressible direction in the crystal has the smallest thermal expansion, and the most compressible direction has the largest thermal expansion. Furthermore, we find that the intermolecular bonds with the largest temperature-dependent changes, those H-bonds donated by interstitial waters to sulphate oxygens, are also the most compressible bonds in the structure.

Generally speaking, the effect of pressure on highly hydrated crystalline salts is to stabilise lower hydrates (e.g., Sood and Stager 1966; Hall and Hamilton 2008; Hamilton and Hall 2008; Oswald et al. 2009). For example, epsomite has been shown experimentally to undergo a series of polymorphic phase transitions below 5 GPa (Fortes et al. 2006a), and we would expect a similar series of transformations in mirabilite, possibly culminating in a transformation to a lower hydrate (either by incongruent melting, or solid-state exsolution of ice), instead of the transformations reported in this paper. However, we *do* expect the general structural trends seen in these simulations to apply to any high-pressure phases of sodium sulphate hydrates, namely the trend towards proton transfer rather than H-bond symmetrisation, the reduction in H-bonds donated to the SO₄ tetrahedron, and a trend towards increasing coordination of the Na cation, including coordination by sulphate oxygens as seen in sodium sulphate octahydrate.

Summary

We have performed the first ab initio DFT calculations on sodium sulphate decahydrate. For the ambient-pressure phase, mirabilite, we have found excellent agreement between the ab initio calculations and experimental structure; the calculated zero-pressure unit-cell volume is over-inflated by approximately 2.2% compared to that measured at 4.2 K by neutron powder diffraction, which is similar to other DFT-GGA computational results we have obtained for hydrogen bonded molecular crystals (e.g., Fortes et al. 2001, 2003a, b, c, 2006b). The agreement with experimentally observed bond lengths and angles, particularly the hydrogen-bond network, is extremely good. The only particular area of difference involves the square H-bonded rings, within which our calculated structure is deliberately missing the partially occupied hydrogen sites.

Our calculations have been used to determine the coefficients of the elastic stiffness tensor in the range $-2.7 < P < 61$ GPa. Mirabilite undergoes phase changes at around 7.5 GPa (characterised by a change in the water molecules forming the primary sixfold coordination polyhedron around one of the sodium cations) and at around 20 GPa (characterised by a change from sixfold to sevenfold coordination of both of the sodium cations by water

molecules). Both transitions involve re-organisation of the hydrogen-bond network. In the pressure range 7.5–20 GPa there are at least two competing metastable structures which have very similar energies and similarly-coordinated Na cations, but distinct sulphate tetrahedron coordination numbers. Structural changes continue in the high-pressure phase, resulting in a series of proton transfers and the formation of H₃O⁺ and OH⁻ ions.

Acknowledgments HEAB was funded by a postgraduate studentship from the Natural Environment Research Council; grant number NER/S/A/2005/13554. Computational resources were provided by the UK Mineral Physics Consortium. ADF acknowledges funding from the Science and Technology Facilities Council (STFC), U.K., grant number PP/E006515/1.

References

- Birch F (1952) Elasticity and constitution of the Earth's interior. *J Geophys Res* 57:227–286. doi:10.1029/JZ057i002p00227
- Blöchl PE (1994) Projector augmented-wave method. *Phys Rev B* 50:17953–17979. doi:10.1103/PhysRevB.50.17953
- Block EA (1913) Über die schmelzkurven einiger stoffe. *Z Phys Chem Stoich Verwandt* 82:403–438
- Botti A, Bruni F, Imberti S, Ricci MA, Soper AK (2004) Ions in water: the microscopic structure of concentrated NaOH solutions. *J Chem Phys* 120:10154–10162. doi:10.1063/1.1705572
- Brand HEA, Fortes AD, Wood IG, Alfredsson M, and Vočadlo L (2006) High-pressure properties of planetary sulfate hydrates determined from interatomic potential calculations. *Lunar Planet Sci Conf 37*, abstract #1310. <http://www.lpi.usra.edu/meetings/lpsc2006/pdf/1310.pdf>
- Brand HEA, Fortes AD, Wood IG, Knight KS, Vočadlo L (2009) The thermal expansion and crystal structure of mirabilite (Na₂SO₄·10D₂O) from 4.2–300 K, determined by time-of-flight neutron powder diffraction. *Phys Chem Min* 36:29–46. doi:10.1007/s00269-008-0256-0
- Brodale GE, Giauque WF (1958) The heat of hydration of sodium sulphate. Low temperature heat capacity and entropy of sodium sulphate decahydrate. *J Am Chem Soc* 80:2042–2044. doi:10.1021/ja01542a003
- Carlson RW, Calvin W, Dalton JB, Hansen GB, Hudson R, Johnson RE, McCord TB, and Moore MH (2007) Europa's surface compositions: what we know, what we would like to know, and how we can find out. *EOS Trans Am Geophys Union* 88(54), Fall Meeting Suppl., abstract P51E-02
- Colman SM, Kelts KR, Dinter DA (2002) Depositional history and neotectonics in Great Salt Lake, Utah, from high-resolution seismic stratigraphy. *Sed Geol* 148:61–78. doi:10.1016/S0037-0738(01)00210-X
- Dalton JB III (2007) Linear mixture modelling of Europa's non-ice material based on cryogenic laboratory spectroscopy. *Geophys Res Lett* 34:L21205. doi:10.1029/2007GL031497
- Dalton JB, Prieto-Ballesteros O, Kargel JS, Jamieson CS, Jolivet J, Quinn R (2005) Spectral comparison of heavily hydrated salts with disrupted terrains on Europa. *Icarus* 177:472–490. doi:10.1016/j.icarus.2005.02.023
- Dougherty AJ, Hogenboom DL, Kargel JS, and Zheng YF (2006) Volumetric and optical studies of high pressure phases of Na₂SO₄·10H₂O with applications to Europa. *Lunar and Planetary Science conference*, 37, #1732

- Finger LW, Kroecker M, Toby BH (2007) DRAWxtl, an open-source computer program to produce crystal structure drawings. *J Appl Cryst* 40:188–192. doi:10.1107/S0021889806051557
- Fortes A (2004) Computational and experimental studies of solids in the ammonia-water system. Dissertation, University of London, p 230
- Fortes AD, Wood IG, Brodholt JP, Vočadlo L (2001) Ab initio simulation of ammonia monohydrate ($\text{NH}_3\cdot\text{H}_2\text{O}$) and ammonium hydroxide (NH_4OH). *J Chem Phys* 115:7006–7014. doi:10.1063/1.1398104
- Fortes AD, Wood IG, Brodholt JP, Vočadlo L (2003a) Ab initio simulation of the ice II structure. *J Chem Phys* 119:4567–4572. doi:10.1063/1.1593630
- Fortes AD, Wood IG, Brodholt JP, Vočadlo L (2003b) Hydrogen bonding in solid ammonia from density-functional theory calculations. *J Chem Phys* 118:5987–5994. doi:10.1063/1.1555630
- Fortes AD, Wood IG, Brodholt JP, Vočadlo L (2003c) The structure, ordering, and equation of state of ammonia dihydrate ($\text{NH}_3\cdot 2\text{H}_2\text{O}$). *Icarus* 162:59–73. doi:10.1016/S0019-1035(02)00073-8
- Fortes AD, Wood IG, Vočadlo L, Brand HEA, Grindrod PM, Joy KH, and Tucker MG (2006a) The phase behaviour of epsomite ($\text{MgSO}_4\cdot 7\text{H}_2\text{O}$) to 50 kbar: planetary implications. *Lunar Planet Sci Conf 37*, abstract #1029. <http://www.lpi.usra.edu/meetings/lpsc2006/pdf/1029.pdf>
- Fortes AD, Wood IG, Alfredsson M, Vočadlo L, Knight KS (2006b) The thermoelastic properties of $\text{MgSO}_4\cdot 7\text{D}_2\text{O}$ (epsomite) from powder neutron diffraction and ab initio calculations. *Eur J Mineral* 18:449–462. doi:10.1127/0935-1221/2006/0018-0449
- Fortes AD, Wood IG, Knight KS (2006c) Neutron powder diffraction studies of sulfuric acid hydrates. I: The structure of sulfuric acid hemitrisikaidekahydrate, $\text{D}_2\text{SO}_4\cdot 6\frac{1}{2}\text{D}_2\text{O}$. *J Chem Phys* 125:144510. doi:10.1063/1.2356860
- Fortes AD, Grindrod PM, Trickett SK, Vočadlo L (2007a) Ammonium sulfate on Titan: possible origin and role in cryovolcanism. *Icarus* 188:139–153. doi:10.1016/j.icarus.2006.11.002
- Fortes AD, Wood IG, Alfredsson M, Vočadlo L, Knight KS, Marshall WG, Tucker MG, Fernandez-Alonso F (2007b) The high-pressure phase diagram of ammonia dihydrate. *High Press Res* 27:201–212. doi:10.1080/08957950701265029
- Fortes AD, Wood IG, Vočadlo L, Knight KS (2008a) Neutron diffraction studies of sulfuric acid hydrates. II: The structure, thermal expansion, incompressibility and polymorphism of sulfuric acid tetrahydrate ($\text{D}_2\text{SO}_4\cdot 4\text{D}_2\text{O}$). *J Chem Phys* 128:054506. doi:10.1063/1.2827474
- Fortes AD, Wood IG, Vočadlo L, Knight KS, Marshall WG, Tucker MG, and Fernandez-Alonso F (2009) Phase behaviour and thermoelastic properties of perdeuterated ammonia hydrate and ice polymorphs from 0 to 2 GPa. *J Appl Cryst* 42:846–866. doi:10.1107/S0021889809027897
- Fortes AD, Wood IG, and Knight KS (2008b) The crystal structure and thermal expansion tensor of $\text{MgSO}_4\cdot 11\text{D}_2\text{O}$ (meridianiite) determined by neutron powder diffraction *Phys Chem Min* 35:207–221. doi:10.1007/s00269-008-0214-x
- Geller A (1924) Über das Verhalten verschiedener minerale der salzlager bei hohen drucken und wechselnden temperaturen. *Z Krist* 60:415–472
- Giguère PA (1983) Les liaisons hydrogène dans les solutions aqueuses d'alcalis. *Rev Chim Min* 20:588–594
- Glauber JH (1658) *Tractatus de natura salium*. Amsterdam
- Goudie AS, Viles H (1997) *Salt weathering hazards*. Wiley, Chichester
- Hall C, Hamilton A (2008) The heptahydrate of sodium sulfate: does it have a role in terrestrial and planetary geochemistry? *Icarus* 198:277–279. doi:10.1016/j.icarus.2008.07.001
- Hamilton A, Hall C (2008) Sodium sulfate heptahydrate: a synchrotron energy-dispersive diffraction study of an elusive metastable hydrated salt. *J Anal Atom Spectrom* 23:840–844. doi:10.1039/b716734b
- Hardie LA (1991) On the significance of evaporites. *Ann Rev Earth Planet Sci* 19:131–168. doi:10.1146/annurev.ea.19.050191.001023
- Hazen RM, Finger LW (1979) Bulk modulus-volume relationship for cation–anion polyhedra. *J Geophys Res* 84:6723–6728. doi:10.1029/JB084iB12p06723
- Hazen RM, Downs RT, Prewitt CT (2000) Principles of comparative crystal chemistry. *Reviews in Mineralogy and Geochemistry*, vol 41. Mineralogical Society of America, Washington DC
- Hermida-Ramon JM, Karlström G (2004) Study of the hydronium ion in water. A combined quantum chemical and statistical mechanical treatment. *J Mol Struct Theochem* 712:167–173. doi:10.1016/j.theochem.2004.10.017
- Hogenboom DL, Kargel JS, and Pahalawatta PV (1999) Densities and Phase relationships at high pressures of the sodium sulfate-water system. *Lunar and Planetary Science conference 30*, abstract #1793
- Hohenberg P, Kohn W (1964) Inhomogenous electron gas. *Phys Rev* 136:B864–B871. doi:10.1103/PhysRev.136.B864
- Kargel JS (1991) Brine volcanism and the interior structure of asteroids and icy satellites. *Icarus* 94:369–390. doi:10.1016/0019-1035(91)90235-L
- Keys JR, Williams K (1981) Origin of crystalline, cold desert salts in the McMurdo region, Antarctica. *Geochim Cosmochim Acta* 45:2299–2309. doi:10.1016/0016-7037(81)90084-3
- Kohn W, Sham LJ (1965) Self-consistent equations including exchange and correlation effects. *Phys Rev* 140:A1133–A1138. doi:10.1103/PhysRev.140.A1133
- Kresse G, Furthmüller J (1996) Efficient iterative schemes for ab initio total-energy calculations using a plane-wave basis set. *Phys Rev B* 54:11169–11186. doi:10.1103/PhysRevB.54.11169
- Kresse G, Joubert J (1999) From ultrasoft pseudopotentials to the projector augmented method. *Phys Rev B* 59:1758–1775. doi:10.1103/PhysRevB.59.1758
- Kryukov PA, Manikhin VI (1960) Characteristics of the melting of Glauber salt at high pressures. *Russ Chem Bull* 9:2077–2078. doi:10.1007/BF00912067
- Langlet J, Bergès J, Reinhardt P (2004) An interesting property of the Perdew–Wang 91 density functional. *Chem Phys Lett* 396:10–15. doi:10.1016/j.cplett.2004.07.093
- Levy HA, Lisensky GC (1978) Crystal structures of sodium sulfate decahydrate (Glauber's salt) and sodium tetraborate decahydrate (borax). Redetermination by neutron diffraction. *Acta Cryst Sect B Struct Sci* 34:3502–3510. doi:10.1107/S0567740878011504
- Markovitch O, Agmon N (2007) Structure and energetics of the hydronium hydration shells. *J Phys Chem A* 111:2253–2256. doi:10.1021/jp068960g
- Marliacy P, Solimando R, Bouroukba M, Schuffenecker L (2000) Thermodynamics of crystallization of sodium sulfate decahydrate in $\text{H}_2\text{O}\text{--}\text{NaCl}\text{--}\text{Na}_2\text{SO}_4$: application to $\text{Na}_2\text{SO}_4\cdot 10\text{H}_2\text{O}$ -based latent heat storage materials. *Thermochim Acta* 344:85–94. doi:10.1016/S0040-6031(99)00331-7
- Marzal RME, Scherer GW (2008) Crystallisation of sodium sulfate salts in limestone. *Environ Geol* 56:605–621. doi:10.1007/s00254-008-1441-7
- McCarthy AC (2007) Behavior of sodium clinopyroxenes under compression. Dissertation, University of Arizona
- Monkhorst HJ, Pack JD (1976) Special points for Brillouin-zone integrations. *Phys Rev B* 13:5188–5192. doi:10.1103/PhysRevB.13.5188
- Ohno H, Igarashi M, Hondoh T (2006) Characterisation of salt inclusions in polar ice from Dome Fuji, East Antarctica. *Geophys Res Lett* 33:L075050. doi:10.1029/2006GL025774

- Orlando TM, McCord TB, Grieves GA (2005) The chemical nature of Europa's surface material and the relation to a subsurface ocean. *Icarus* 177:528–533. doi:[10.1016/j.icarus.2005.05.009](https://doi.org/10.1016/j.icarus.2005.05.009)
- Oswald ID, Hamilton H, Hall C, Marshall WG, Prior TJ, Pulham CR (2009) In situ characterization of elusive salt hydrates—the crystal structure of the heptahydrate and octahydrate of sodium sulfate. *J Am Chem Soc* 130:17795–17800. doi:[10.1021/ja805429m](https://doi.org/10.1021/ja805429m)
- Palache C, Berman H, Frondel C (1951) Dana's system of mineralogy, 7th edn, vol II. pp 439–442
- Perdew JP (1991) In: Zeische P, Eschrig H (eds) *Electronic structure of solids*. Akademie, Berlin
- Perdew JP, Wang Y (1992) Accurate and simple analytic representation of the electron–gas correlation energy. *Phys Rev B* 45:13244–13249. doi:[10.1103/PhysRevB.45.13244](https://doi.org/10.1103/PhysRevB.45.13244)
- Pickard CJ, Needs RJ (2008) Highly compressed ammonia forms an ionic crystal. *Nat Geosci* 7:775–779. doi:[10.1038/nmat2261](https://doi.org/10.1038/nmat2261)
- Poirier JP, Tarantola A (1998) A logarithmic equation of state. *Phys Earth Planet Inter* 109:1–8. doi:[10.1016/S0031-9201\(98\)00112-5](https://doi.org/10.1016/S0031-9201(98)00112-5)
- Putz H, Schoen JC, Jansen M (1999) Combined method for “ab initio” structure solution from powder diffraction data. *J Appl Cryst* 32:864–870. doi:[10.1107/S0021889899006615](https://doi.org/10.1107/S0021889899006615)
- Rijniers LA, Huinink HP, Pel L, Kopinga K (2005) Experimental evidence of crystallisation pressure inside porous media. *Phys Rev Lett* 94:075503. doi:[10.1103/PhysRevLett.94.075503](https://doi.org/10.1103/PhysRevLett.94.075503)
- Ripmeester JA, Ratcliffe CI, Dutrizac JE, Jambor JL (1986) Hydrogenium ion in the alunite-jarosite group. *Can Min* 24:435–447
- Ruben HW, Templeton DH, Rosenstein RD, Olovsson I (1961) Crystal structure and entropy of sodium sulfate decahydrate. *J Am Chem Soc* 83:820–824. doi:[10.1021/ja01465a019](https://doi.org/10.1021/ja01465a019)
- Sood RR, Stager RA (1966) Pressure-induced dehydration reactions and transitions in inorganic hydrates. *Science* 154:388–390. doi:[10.1126/science.154.3747.388](https://doi.org/10.1126/science.154.3747.388)
- Tammann G (1929) Über die Schmelzkurven einiger Salzhydrate. *Z Anorg Allgem Chem* 178:309–316. doi:[10.1002/zaac.19291790114](https://doi.org/10.1002/zaac.19291790114)
- Tanaka Y, Hada S, Makita T, Moritoki M (1992) Effect of pressure on the solid–liquid phase equilibria in (water + sodium sulfate) system. *Fluid Phase Equil* 76:163–173. doi:[10.1016/0378-3812\(92\)85085-M](https://doi.org/10.1016/0378-3812(92)85085-M)
- Tsui N, Flatt RJ, Scherer GW (2003) Crystallization damage by sodium sulphate. *J Cult Heritage* 4:109–115. doi:[10.1016/S1296-2074\(03\)00022-0](https://doi.org/10.1016/S1296-2074(03)00022-0)
- Tsuzuki S, Lüthi HP (2001) Interaction energies of van der Waals and hydrogen bonded systems calculated using density functional theory: assessing the PW91 model. *J Chem Phys* 114:3949–3957. doi:[10.1063/1.1344891](https://doi.org/10.1063/1.1344891)
- Wallace DG (1998) *Thermodynamics of crystals*. Dover, New York
- Wang Y, Perdew JP (1991) Correlation hole of the spin-polarized electron gas, with exact small-wave-vector and high-density scaling. *Phys Rev B* 44:13298–13307. doi:[10.1103/PhysRevB.44.13298](https://doi.org/10.1103/PhysRevB.44.13298)